

# Exploring disk galaxy dynamics using IFU data

E. Noordermeer,<sup>1</sup> M. R. Merrifield<sup>1\*</sup> and A. Aragón-Salamanca<sup>1</sup>

<sup>1</sup>*University of Nottingham, School of Physics and Astronomy, University Park, NG7 2RD Nottingham, UK*

2 November 2018

## ABSTRACT

In order to test the basic equations believed to dictate the dynamics of disk galaxies, we present and analyze deep two-dimensional spectral data obtained using the PPAK integral field unit for the early-type spiral systems NGC 2273, NGC 2985, NGC 3898 and NGC 5533. We describe the care needed to obtain and process such data to a point where reliable kinematic measurements can be obtained from these observations, and a new more optimal method for deriving the rotational motion and velocity dispersions in such disk systems. The data from NGC 2273 and NGC 2985 show systematic variations in velocity dispersion with azimuth, as one would expect if the shapes of their velocity ellipsoids are significantly anisotropic, while the hotter disks in NGC 3898 and NGC 5533 appear to have fairly isotropic velocity dispersions. Correcting the rotational motion for asymmetric drift using the derived velocity dispersions reproduces the rotation curves inferred from emission lines reasonably well, implying that this correction is quite robust, and that the use of the asymmetric drift equation is valid. NGC 2985 is sufficiently close to face on for the data, combined with the asymmetric drift equation, to determine all three components of the velocity ellipsoid. The principal axes of this velocity ellipsoid are found to be in the ratio  $\sigma_z : \sigma_\phi : \sigma_R \approx 0.7 : 0.7 : 1$ , which shows unequivocally that this disk distribution function respects a third integral of motion. The ratio is also consistent with the predictions of epicyclic theory, giving some confidence in the application of this approximation to even fairly early-type disk galaxies.

**Key words:** galaxies: spiral – galaxies: kinematics and dynamics – galaxies: individual: NGC 2273, NGC 2985, NGC 3898, NGC 5533

## 1 INTRODUCTION

Disk galaxies are fundamentally dynamical entities, so any understanding of their structure must pay as much attention to the velocities of their constituent stars as it does to their positions. This kinematic information is usually collected through spectroscopy, where the mean shift and broadening of spectral lines provides information on the line-of-sight mean velocities and velocity dispersions of the stellar population that produced the light. In the past, such spectra have typically been obtained through long-slit spectrographs, where a one-dimensional cut through the galaxy is dispersed in the second dimension on a two-dimensional detector.

Over the years, such data have provided a number of useful insights into the dynamical properties of these systems. For example, observations along the major axes of inclined disk galaxies have demonstrated that the stellar component rotates more slowly than each system’s circular speed (van der Kruit & Freeman 1986; Bottema et al.

1987). This “asymmetric drift” is exactly what one expects if the stars also have significant random velocities, so that the radial structure of the galaxy is not entirely supported against gravity by its rotational motion. Similarly, observations of face-on systems have shown that the vertical component of the random velocity decreases with radius in the manner that one might expect if disks are to maintain a constant scale-height in the presence of radially-decreasing self-gravitation (van der Kruit & Freeman 1986).

However, the one-dimensional spatial data provided by such long-slit observations have some serious limitations. First, these data provide information on only two dimensions (the spatial one and the line-of-sight velocity) of the intrinsically six-dimensional phase space of a galaxy. This lack of dimensional coverage can be ameliorated by obtaining long-slit data from a variety of position angles. For example, Gerssen et al. (1997) obtained data along both the major and minor axes of the disk galaxy NGC 488 to infer the relative amplitudes of random motions in two different directions within this system. Combining these observations with a physical assumption, such as the “epicycle approximation” which ties random motions in the radial and az-

\* email: michael.merrifield@nottingham.ac.uk

azimuthal directions together (Binney & Tremaine 1987), then allowed the solution for the full three-dimensional distribution of random velocities in the disk of this galaxy. However, even such multiple cuts are clearly spatially incomplete and provide a rather inefficient approach to acquiring kinematic data. This problem is compounded by the very faint nature of the outer parts of disk galaxies, which necessitates long integrations for even a single slit orientation.

A major step forward came with the development of large-area integral field units (IFUs), which provide spectral coverage across a full two-dimensional field of view. These instruments have revolutionized our view of elliptical systems through studies such as those undertaken with the SAURON spectrograph (Emsellem et al. 2004). Results on the dynamical properties of disk systems have been somewhat slower to emerge, although some studies are now beginning to bear fruit (e.g. Westfall et al. 2008). Partly this slower progress arises from the rather subtler nature of disk galaxy dynamics, as the much smaller random motions in these systems makes the basic measurements of line broadening more challenging and prone to systematic error. Further, the more complex geometry of these systems, with multiple components, spiral structure, etc, renders the interpretation of these data a great deal more difficult.

The potentially-rapid spatial variations in the kinematics of these systems present particular challenges since the conventional approach involves averaging together spectra from quite large regions of the galaxy to obtain a sufficiently high signal-to-noise ratio to obtain meaningful kinematic measurements. Such averaging will smooth out any fine structure in the kinematics and may even introduce significant biases into the analysis. For example, Westfall et al. (2008) have recently found that their previous analysis systematically over-estimated the measurement of some components of random motion because the spatial averaging over a range of azimuthal angles combined data with different mean-streaming and random motions, creating an artificial broadening of the intrinsic velocity distribution. Given these difficulties, it is not obvious what the optimum approach is for deriving even the most basic kinematic parameters from such two-dimensional data. For instance, at any given radius, as one looks around in azimuth away from the major axis, there is still clearly significant information within the data on the mean streaming motions of the stars at that radius, but since the projection of that mean streaming motion into the line of sight varies with azimuth one cannot simply average the spectra to measure it.

In addition, some of the physical assumptions that have been used in the interpretation of such kinematic data are somewhat controversial. The frequently-adopted epicycle approximation, for example, is strictly only valid when the stars' departures from circular motions are very small. Westfall et al. (2008) state that their tests show that this condition is adequately met in the outer parts of all credible disk galaxies, but Kuijken & Tremaine (1994) found that even for the relatively small amplitude of random motions in a "cold" disk environment like the solar neighbourhood of the Milky Way, this condition is not sufficiently met, and the resulting error is at the 20 – 40% level.

Even the more generally applicable asymmetric drift equation can only be used if a number of assumptions are made. It is, for example, often assumed that the random

motions decrease smoothly and exponentially with radius, to force the derivatives of these quantities to be well behaved. Although this assumption is supported by observation of a number of systems (e.g. van der Kruit & Freeman 1986; Bottema 1993; Gerssen et al. 1997) including our own galaxy (Lewis & Freeman 1989), it is now known that in some cases the random motions do not vary with radius in this simple manner in disk systems (e.g. Merrett et al. 2006; Noordermeer et al. 2008). The applicability of this equation has broader implications, since the correction for asymmetric drift has been used to estimate the circular speeds of S0 galaxies for which no emission-line rotation curves exist (Bedregal, Aragón-Salamanca, Merrifield & Milvang-Jensen 2006). These circular speeds have then been used to study the Tully–Fisher relation for these systems to determine whether they are simply faded spiral galaxies (Bedregal, Aragón-Salamanca & Merrifield 2006). If it turns out that the asymmetric drift correction does not provide a robust way to estimate circular speeds for these fairly "hot" disks, then such techniques for inferring the life histories of S0 systems are brought into serious question.

In this paper, we revisit all these issues with a view to creating and testing a more robust framework for analyzing the kinematics of disk galaxies, and testing the assumptions that go into analyzing their dynamics. In Section 2, we describe the selection of a sample of four fairly early-type disk galaxies. As such, their observed kinematics are not contaminated by strong localized spiral features, so we can restrict this first analysis of disk galaxy dynamics to their more global properties. In addition, their early types mean that they are directly comparable to S0 systems, allowing us to test the validity of asymmetric drift corrections for such galaxies. However, they are all also chosen to display good emission-line rotation curves, so that we have direct comparators for the dynamically-inferred stellar rotation curves. Section 2 also describes the rather careful observations undertaken using the PPAK IFU on the Calar Alto 3.5m Telescope to minimize systematic errors in the requisite high-quality spectral data, and Section 3 presents the manner in which these data were reduced while taking care to preserve the dynamical signal in an uncompromised form. Section 4 introduces a new technique for extracting in a more optimal manner the mean streaming velocity and random motions from such two-dimensional data, and presents the resulting inferred kinematics. Section 5 explores the dynamics that can be derived from these data, discussing the shape of the velocity ellipsoid, and the validity of both the asymmetric drift equation and the epicycle approximation. Finally, we draw some conclusions in Section 6.

## 2 SAMPLE SELECTION AND OBSERVATIONS

### 2.1 Sample selection

Since the intention of this study is to investigate the viability of measuring the large-scale stellar dynamics of disk systems, we have targeted early-type disk galaxies that do not contain significant confusing spiral structure. In addition, these systems are sufficiently early in the Hubble sequence to be comparable to S0 galaxies, since we are seeking to ascertain whether one can correct for asymmetric

**Table 1.** Sample galaxies: basic data

Name	Type	D	$L_R$	$\mu_{0,R}$	$B - R$	$v_{\max}$	$v_{\text{asympt}}$	$i$
(1)	(2)	Mpc	$10^{10} L_{\odot}$	$\frac{\text{mag}}{\text{arcsec}^2}$	mag	$\text{km s}^{-1}$	$\text{km s}^{-1}$	$^{\circ}$
(1)	(2)	(3)	(4)	(5)	(6)	(7)	(8)	(9)
NGC 2273	SB(r)a	27.3	1.84	15.84	1.5	260	190	55
NGC 2985	(R')SA(rs)ab	21.1	3.05	15.56	1.1	255	220	37
NGC 3898	SA(s)ab	18.9	1.72	15.35	1.3	270	250	69
NGC 5533	SA(rs)ab	54.3	5.92	16.27	1.4	300	230	53

*Notes* – Col. (1), name; Col. (2), morphological type; Col. (3), distance (based on Hubble flow, corrected for Virgo-centric inflow and assuming  $h=0.75$ ); Cols (4) and (5), R-band total luminosity and central surface brightness (corrected for Galactic foreground extinction); Col. (6)  $B - R$  colour; Cols. (7) and (8), maximum and asymptotic rotation velocities; Col. (9) inclination. Col. (2) from NASA Extragalactic Database; Col. (3) from Noordermeer et al. (2005); Cols (4) – (6) from Noordermeer & van der Hulst (2007); and Cols (7) – (9) from N07.

drift in such potentially-hot disks. However, we also require sufficient gas in each system for there to be a reliable emission-line rotation curve for comparison, so we have selected galaxies from the gas-rich early-type disk galaxy sample of Noordermeer et al. (2007, hereafter N07), for which high-quality rotation curves have already been derived using HI observations and long-slit optical emission line spectra.

In addition, we restricted the selection to galaxies that:

- (i) are visible from Calar Alto at the time of observation;
- (ii) are large enough on the sky for us to co-add many spectra to obtain adequate signal;
- (iii) are small enough on the sky to fit most of the light of the galaxy within two pointings of the PPAK IFU;
- (iv) are inclined at an inclination of  $i \gtrsim 40^{\circ}$  in order to ensure that rotational motion and other in-plane velocities are observable in the line-of-sight velocities;
- (v) are inclined at an inclination of  $i \lesssim 70^{\circ}$  in order to resolve the minor axis of the system and to avoid extreme projection effects along the line of sight.

The basic properties of the four galaxies in this study, selected by these criteria, are presented in Table 1.

## 2.2 Observations

The galaxies in the sample were observed with the fibre-based integral-field unit PPAK, mounted on the PMAS spectrograph of the German–Spanish 3.5m telescope at Calar Alto Observatory. The PPAK unit comprises 331 fibres, each with a diameter on the sky of  $2.7''$ , packed in a hexagonal grid with minimum and maximum diameters of 64 and  $74''$  respectively; the large field of view of this IFU makes it very well-suited to studies of nearby galaxies. An additional 36 fibres (6 groups of 6 fibres each) are placed at a distance of  $72''$  from the IFU centre and can, as long as they are not polluted by light from the main object, be used to sample the surrounding sky. Finally, 15 fibres are not illuminated from the sky, but are connected to a calibration unit. These calibration fibres can be illuminated with light from lamps during the science exposures, allowing synchronous spectral calibration, which is important in correcting for flexure between exposures, to prevent such systematic problems from compromising the measured velocity dispersions. A more detailed description of the PPAK fibre-unit is provided by Kelz et al. (2006).

The PPAK unit feeds the spectra from all fibres into

the PMAS spectrograph. To achieve the desired spectral resolution, we used the J1200 grating in second order and in ‘backward blaze’ (Roth et al. 2005; Kelz et al. 2006). By rotating the grating appropriately, a spectral window of  $4950\text{\AA} - 5400\text{\AA}$  was selected, covering the Mg b  $5175\text{\AA}$  absorption lines and many surrounding weaker iron features. The spectral resolution with this setup is about 8200, corresponding to a FWHM wavelength resolution at our central wavelength of  $0.63\text{\AA}$ . In practice, the spectral resolution was found to vary systematically with position on the detector chip, presumably caused by a slight tilt of the detector in the focal plane, and the average effective resolution as measured from our final spectra was approximately  $0.8\text{\AA}$  (FWHM), corresponding to an instrumental velocity dispersion of  $20 \text{ km s}^{-1}$ . As we describe below, these variations in resolution with position were dealt with in the data reduction to prevent the introduction of systematic biases in the measured velocity dispersions.

The observations were carried out under photometric conditions on the nights 2007 January 17 – 20. Even with the large size of the PPAK IFU, the target galaxies were too large to fit in the field of view of the fibre bundle, so each system was observed in two pointings. A few short exposures, giving a total integration times of 1 – 1.5 hours, were taken of the bright, central regions of each galaxy, while multiple longer exposures, giving total exposure times between 4.5 and 6 hours, were taken at fields along the major axis, offset such that they had a small overlap with the central pointing. A summary of these observations is given in Table 2.

Since the galaxies are large, the IFU’s sky fibres were often contaminated by light from the galaxy, and so would not have been suitable for sky subtraction. We therefore obtained short (300 second) exposures of blank fields before and after the galaxy exposures; by averaging the spectra from these exposures in the fibres that contained no light from foreground stars, high signal-to-noise ratio sky spectra were obtained (see Section 3.4). Further calibration of all these on-sky exposures was obtained by briefly (for typically 5 seconds) illuminating the 15 calibration fibres with a thorium–argon (ThAr) arc lamp, in order to correct for any intra-exposure flexure of the instrument (see Section 3.2).

During the run, a total of 13 velocity template stars were observed (see Table 3). Most stars are of late spectral type (G and K), but an A star and two F stars were also included to ensure that we could construct composite spectra that matched the galaxies. In order to quantify the

**Table 2.** Summary of the observations

galaxy	pointing	observing dates January 2007	total exposure time s	average seeing "	photometric?
NGC 2273	centre	17	3600	1.8	yes
	south-west	17–20	18000	1.3	yes
NGC 2985	centre	17	3600	1.6	yes
	south	18–20	20400	1.1	yes
NGC 3898	centre	17	3600	1.5	yes
	north-west	17–20	21600	1.2	yes
NGC 5533	centre	17	5400	1.4	yes
	south-west	18–20	16500	1.1	yes

**Table 3.** Observed velocity template stars

star name	spectral type
HD 65900	A1 V
HD 137391	F0 V
HD 136202	F8 III–IV
HD 139641	G7.5 IIIb
HD 38656	G8 III
HD 41636	G9 III
HD 28946	K0
HD 135482	K0 III
HD 139195	K0p
HD 23841	K1 III
HD 48433	K1 III
HD 20893	K3 III
HD 102328	K3 III

variation of the spectral resolution with position on the chip (see above), we drifted the telescope in the east–west direction during these exposures, such that we obtained the star spectrum in each fibre along a central row in the IFU (see Figure 1, upper panel). Due to the ordering of fibres in the spectrograph, this sampling also spanned the spectrograph detector (see Figure 1, lower panel), allowing us to calibrate out the variations in spectral resolution with position that would otherwise have compromised our ability to measure velocity dispersions with the necessary accuracy.

Finally, in addition to standard bias frames, two sets of calibration images were taken at the beginning and end of each observing night. First, a series of dome flat exposures was taken using a conventional incandescent lamp. The calibration fibres were simultaneously illuminated with a halogen light-source. The resulting spectra are bright and featureless and are used to define and trace the apertures for the individual fibres over the detector, as well as to correct for fibre-to-fibre throughput variations (see Section 3.3). Second, additional dome flats were obtained using a bright arc lamp, simultaneously illuminating the calibration fibres with the same ThAr lamp as used during the night-time, on-sky exposures. These frames are used to determine the wavelength solution (see Section 3.3).

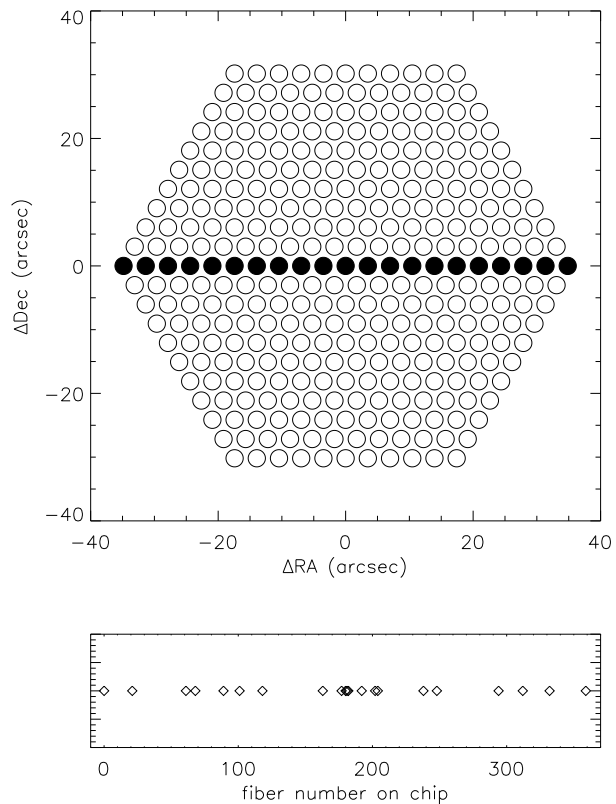


**Figure 1.** Illustration of the drift-scan procedure used for the observation of the template star HD 20893. The top panel shows the illuminated fibres: the telescope was drifted such that the star spectrum is observed in each fibre in the central row. The bottom panel shows the location of the illuminated spectra, which span the detector.

### 3 DATA REDUCTION

#### 3.1 Initial steps

The initial stages in the data reduction were performed within the IRAF environment.<sup>1</sup> The readout bias in each raw image was subtracted using the overscan region of the chip. The remaining structure in the noise was removed using standard bias frames.

To correct for pixel-to-pixel sensitivity variations, we

<sup>1</sup> IRAF is distributed by the National Optical Astronomy Observatories, which are operated by the Association of Universities for Research in Astronomy, Inc., under cooperative agreement with the National Science Foundation.

used a set of special dome flats, kindly provided by Marc Verheijen, taken with the spectrograph so far out of focus that the emission from the individual fibres is smeared out and fills in the inter-fibre regions on the chip. From these frames, a response image was created by fitting a low-order polynomial in the spectral direction and calculating the ratio between the raw image and the fit, thus removing the large-scale spectral shape and the intensity variations between fibre- and inter-fibre-regions from the original images. The individual bias-subtracted images were then divided by this response image.

Bad pixels were identified in the combined bias image, by finding individual pixels as well as entire columns and rows that deviate strongly from their neighbours. Once the bad regions were identified, the corresponding pixels in all other images were corrected by linear interpolation from their neighbours. Finally, an initial pass was made to remove cosmic rays from individual frames using the ‘L.A.Cosmic’ procedure (van Dokkum 2001).

### 3.2 Corrections for flexure

PMAS is known to suffer significantly from flexure, particularly when objects are past the meridian and starting to set (Roth et al. 2005; Verheijen et al. 2004). To mitigate this problem, we only observed galaxies while they were rising. However, it was still important to monitor and correct for any residual flexure. In principle, one could use the ThAr spectra in the 15 calibration fibres for each exposure directly to derive individual distortion corrections and wavelength solutions. However, due to the low signal-to-noise ratio of these spectra, the small number of ThAr lines in our wavelength range and the sparse sampling in the spatial direction (15 calibration fibres for a total of 367 sky spectra), this approach is in practice not viable. Instead, for each on-sky exposure, we compared the positions of a few well-detected emission lines in the calibration fibres with those in the averaged arc-lamp dome flat exposure. The average difference between the positions on both images then gives the linear flexure of the instrument between the dome flats and the on-sky exposure. In practice, these shifts between exposures were found to be only of the order of one pixel or less, and were effectively removed by this procedure. The small size of the effect means that shifts in the wavelength solution during individual exposures would not blur the spectra sufficiently to compromise our ability to determine velocity dispersions accurately.

Once the shift in the calibration ThAr lines between each on-sky exposure and the arc dome flat had been determined, new arc and dome flat images were created, shifted to match the on-sky images. This approach is preferred to shifting the on-sky data since the dome flat images have much higher signal-to-noise ratios, so are not compromised by this sub-pixel interpolated shift. Thus, each on-sky image ends up with its own calibration images, corrected for any flexure present at its particular telescope orientation.

### 3.3 Extraction and calibration of the spectra

The HYDRA package in IRAF was used to extract and calibrate the spectra from the individual fibres. First, the aper-

ture for each fibre was determined using the continuum-lamp dome flat (corrected for flexure as described above). An identification table was used to distinguish between object, sky and calibration fibres. The continuum-lamp spectra were traced along the spectral direction, and a function fitted to describe the fibre positions on the chip. The dome flat spectra were then extracted and their relative intensities used to determine the fibre-to-fibre throughput variations. Similarly, the arc-lamp spectra (corrected for flexure) were extracted using the same positional fit, the lines in the spectra were identified, and a solution produced by fitting a low-order polynomial to describe wavelength as a function of position in the spectrum. Finally, the object spectra were extracted with the same spatial trace, and were re-binned to a logarithmic wavelength scale based on the derived spectral calibration.

To assess independently the accuracy of these wavelength calibrations, we measured the wavelengths of a number of sky lines in a selection of the final spectra. We found excellent agreement with the literature wavelengths, with a negligible mean offset and an RMS scatter of  $0.05\text{\AA}$ , corresponding to an insignificant velocity error of  $3\text{ km s}^{-1}$ .

### 3.4 Sky subtraction

For the subtraction of the contribution of the sky to our template star spectra, we averaged the spectra from all fibres which were not illuminated by the star. For the galaxy spectra, we averaged all spectra from the corresponding separate sky exposure (again rejecting any fibres which were contaminated by foreground stars) and rescaled according to the exposure time of the latter. The resulting sky spectra were then subtracted from each individual spectrum to yield a set of cleaned and fully calibrated spectra.

### 3.5 Final steps

The final step in the data reduction process was to combine the individual exposures of the same fields to increase the signal-to-noise ratio and to reject residual cosmic rays and bad pixels that had not been removed in the previous steps. Thus, the end result of the reductions are, for each galaxy, two sets of fully cleaned and calibrated spectra, one for each pointing.

To facilitate this step, we used the ‘Euro3D Visualisation Tool’ (Sánchez 2004) to display the reduced spectral and spatial data as a cube and to visually inspect features in the spectra. The software requires as additional input a table describing the position of the 331 fibres in the central hexagon on the sky, which was kindly provided to us by the Calar Alto staff. This tool also allowed us to make interpolated 2D images of the integrated continuum emission in each pointing. The images for the central pointings were then registered to the R-band images from Noordermeer & van der Hulst (2007) to accurately determine the centre of the galaxies in all these pointings, thus allowing the creation of a single registered stacked spectral data cube.

For the off-centre pointings of the galaxies, there was generally too little structure in the continuum brightness distribution to register accurately to the R-band images,

so for these we used the recorded telescope offsets between the central and the off-centre pointings instead. Using those cases where there was an appropriate calibrator (such as a foreground star), we found that the error in these offsets was significantly smaller than a fibre diameter, and is entirely adequate for the purposes of measuring the large-scale dynamics of these systems. Figure 2 shows the resulting spatial coverage of the pair of pointing on each galaxy, and the reconstructed image that one obtains by collapsing the spectra into an integrated light measurement.

#### 4 INFERRING THE KINEMATICS

Having produced a set of fully calibrated spectra, we are now in a position to infer each galaxy’s kinematic properties. As highlighted in the Introduction, the issues in studies of disk galaxies are rather different from those in elliptical systems for two reasons. First, the signals are rather subtler in that the random motions, although critical to understanding the dynamics of these systems, are relatively small so must be extracted with care. Second, the observable kinematics can vary quite rapidly with position, so one must also be careful when averaging together data to obtain adequate signal-to-noise ratios that one does not wash out these signals in a destructive manner. To deal with these issues, we have adapted some existing software and developed some new algorithms, as we now describe.

##### 4.1 Fitting technique

Before getting to the details of how we combine data to obtain the requisite signal-to-noise ratio spectra, we must first choose an appropriate method for extracting kinematic parameters and errors from such spectra, since this part of the process will inform us as to the signal-to-noise ratios required in the combined data. After some experimentation, we adopted the Penalized Pixel Fitting Method (PPXF) from Cappellari & Emsellem (2004) to measure the velocity shift and dispersion, since it proved robust and effective. For each spectrum, this method finds the linear combination of velocity template star spectra and the velocity shift and dispersion which together best reproduce the observed spectrum. Although this technique will also fit higher-order moment terms given high-enough quality spectra, since we are primarily interested in the velocity dispersion, and since we are seeking to minimize the amount of averaging required to obtain robust results, here we do not try to constrain these terms.

As described in Section 2.2, the spectral resolution in these observations varied systematically with fibre position on the chip. For the derivation of the velocity shifts, this effect is of little importance, but for measuring velocity dispersions it could potentially introduce large systematic errors. Thus, when determining velocity dispersions, we take into account the position of each fibre on the CCD. Whenever we combine fibres from different positions on the chip to create an averaged galaxy spectrum, we create an associated composite stellar template by combining the stellar spectra obtained from the same parts of the detector with the same weighting. This matched approach ensures that

the stellar template has the same effective instrumental resolution as the galaxy spectrum, so that the inferred velocity dispersion is intrinsic to the galaxy, with no artificial contribution due to a mismatch in resolution between the galaxy and template spectra.

The errors on the derived kinematic parameters were determined using Monte-Carlo simulations, in a similar manner to Bedregal et al. (2006). For each fitted spectrum, the RMS residual between the input spectrum and the fit is determined. We then create 100 artificial spectra by adding random noise (with the same RMS as in the observed spectrum) to the fitted spectrum, and measure the velocity shift and dispersion from the simulated spectra. The spread in the simulated values then gives an estimate for the error in the original measurements. In the case of rotational velocity, the errors on the mean velocity must be corrected for the inclination of the galaxy, and the uncertainty in the systemic velocity of the galaxy must also be added in in quadrature.

Note that these random errors do not contain the full error budget, as there may also be systematic errors arising from template mismatch, uncertainty in the assumed inclination, systematic effects arising from non-circular motions in the galaxy which have not been modelled, etc. Nonetheless, they provide a good measure of the uncertainties that arise directly from the quality of the data. They show, for example, that we can obtain reasonably reliable measurements of mean velocity and velocity dispersion from spectra with a signal-to-noise ratio per pixel of at least 20.

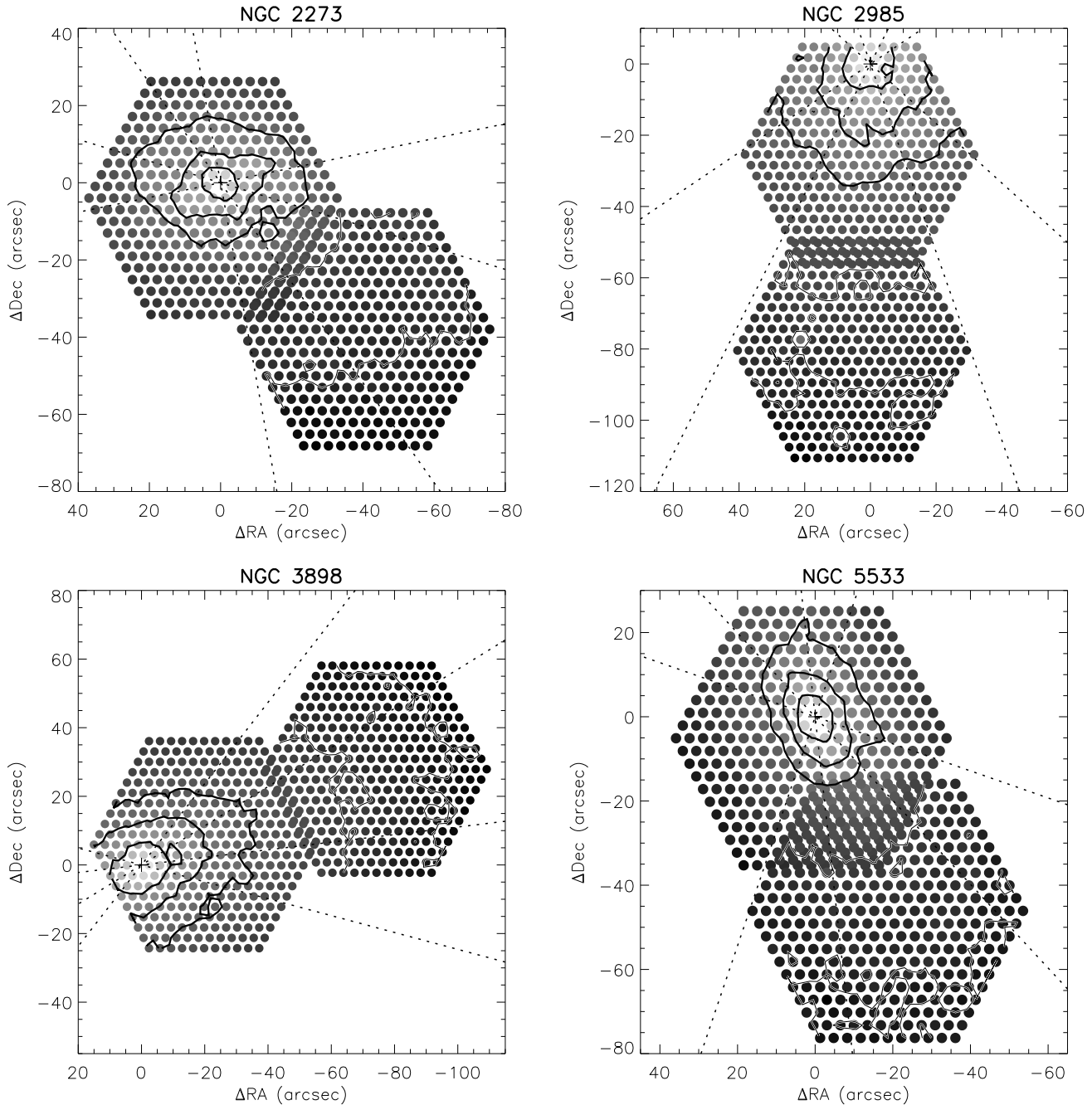
##### 4.2 Stellar rotation curve

Figure 2 illustrates the problem that we face in trying to determine the kinematic properties of these galaxies. It is clear that only the very central fibres have the signal-to-noise ratios in excess of 20 that are required to measure the velocity shift and dispersion from the individual spectra. For all other fibres, we need to combine multiple spectra to increase the signal-to-noise ratio before we can measure, for example, the velocity dispersion.

Before doing this, however, we need to correct for the rotational motions of the stars around the centres of the galaxies. The galaxies in our sample are all characterised by large rotational motions, with maximum velocities of the order of  $250 \text{ km s}^{-1}$  (see Table 1), so that even spectra which have only slightly different azimuthal angles<sup>2</sup> will be shifted to significantly different radial velocities. Thus, even if we simply co-added spectra close to the major axes of our galaxies, we would artificially broaden the absorption lines in the combined spectrum, especially when the ratio between rotational velocity and velocity dispersion is large; for spectra further from the major axes, the effect would be even worse.

Unfortunately, we do not know *a priori* exactly how fast the stars are rotating in order to subtract this shift from the spectra before co-adding them. The gas rotational velocities from N07 give an upper limit only, as the stars will rotate more slowly due to asymmetric drift. The magnitude of this

<sup>2</sup> We define the azimuthal angle  $\phi$  as the angle with respect to the major axis measured in the plane of the disc of the galaxy, so for a non-face-on system it requires a deprojection of the conventional position angle.



**Figure 2.** Reconstructed images of total intensity for the four galaxies in the sample. The dots indicate the brightness of the integrated emission in each fibre, on a logarithmic gray-scale. The sizes of the dots are roughly equal to the true size of the fibres on the sky. The thick black contours show constant signal-to-noise ratios (per  $0.21\text{\AA}$  pixel) of 20, 10 and 5 (from the centre outwards) in the central pointings, while the thin black contours indicate signal-to-noise ratios of 5 and 2 in the outer pointings. The locations of the centres of the galaxies are indicated with the plus-signs. Dotted lines indicate the regions within azimuthal angles of  $30^\circ$  from the major and the minor axes.

offset is at this stage still unknown and is in fact one of the main quantities that we are trying to measure!

We can, however, retrieve the stellar rotation curve from the data by realising that, when we account for the rotational motions correctly in combining spectra, a measurement of velocity dispersion from the combined spectrum will return a true average velocity dispersion for the region over which spectra have been co-added. However, if we do not use the correct rotation velocity and consequently do

not shift the individual spectra correctly, then the resulting co-added spectrum will always be artificially broadened and will generate a spuriously-enlarged velocity dispersion. Based on this effect, we have adopted the following procedure to derive the stellar rotation curve from these data.

First, we divide the spectra into a number of radial bins (with the distance of each fibre to the centre of the galaxy measured in the plane of the disc of the galaxy). The radial extent of these bins were chosen such that we obtain a signal-

to-noise ratio of  $\gtrsim 20$  in all the co-added spectral data that we analyze here and later, which is sufficient to obtain a reliable measure of velocity dispersion averaged over all the regions that we consider. For each radial bin, we consider a large series of possible stellar rotational velocities. For each such velocity, we calculate the line-of-sight velocity shift of each fibre within the bin with respect to the centre of the galaxy, and un-Doppler-shift its spectrum accordingly. One slight subtlety here is that not all spectra contain the same amount of information about the stellar rotation speed, since this motion does not project into the line of sight along a galaxy’s minor axis, so we assign a weight to each spectrum according to its azimuthal angle,  $w_s = |\cos \phi|$ . With this weighting, we then combine all spectra in the radial bin and measure the velocity dispersion and shift of the resulting composite spectrum. As discussed above, the true rotation speed will be the one that returns the minimum measured velocity dispersion, so we can determine the rotation speed in this bin simply by finding the value that minimizes this quantity.

This procedure is illustrated in the left-hand panels of Figure 3, which shows the results obtained for an intermediate-radius bin ( $16'' < R < 25''$ ) in NGC 2273. The curve of velocity dispersion versus assumed rotational velocity shows a clear minimum at a rotation speed of about  $212 \text{ km s}^{-1}$ , and we therefore conclude that this must be the true average rotation velocity at these radii in this galaxy.

The bottom left-hand panel in Figure 3 shows that the measured velocity shift of the composite spectrum, obtained by optimally shifting individual spectra and averaging in azimuth, lies very close to the systemic velocity from N07. This coincidence is to be expected, since, if we have adopted the correct rotational velocity, we have effectively removed the entire rotational component from the data and we have shifted each individual spectrum back to the systemic velocity. In Table 4 we list the systemic velocities for the galaxies in the sample, derived by taking the averages of such values from the individual rings; the errors were estimated from the spread of the results from the individual rings. In each case, there is excellent agreement between our values and the independent velocities from N07. These derived systemic velocities are also indicated in Figure 3.

This procedure works very well for radial bins where the fibres cover at least a nearly full ellipse around the centre of the galaxy, so that the data probe all azimuthal angles. However, as is apparent from Figure 2, we do not have such azimuthal coverage for the outer radii in these galaxies. The right-hand panels of Figure 3 show what happens if we try to apply this method at large radii where the data all lie close to the major axis. In these cases, all the fibres lie at similar azimuthal angles, so are shifted by similar amounts when the rotation correction is applied. As a result, for any assumed rotation velocity, all spectra are shifted by a nearly equal velocity, and the dispersion in the resulting co-added spectrum shows very little variation (top right-hand panel in Figure 3). In this case, the method described above clearly does not have enough leverage to determine the rotation velocity.

Nevertheless, we can still determine the rotational velocities in such situations by considering the data in the bottom right-hand panel of Figure 3. This plot shows that the velocity shift in the co-added spectrum is a linear function

of the assumed rotation velocity. Such a simple form is to be expected as a consequence of the near-equal azimuth of the fibres in this bin: the velocity shifts for all spectra in the bin are nearly equal and there are no spectra on the opposite side of the major axis to compensate in the final co-added spectrum. Thus, the final spectrum has a velocity shift directly proportional to the assumed rotational velocity and the slope of the relation is very nearly equal to  $\sin i$ , where  $i$  is the inclination of the galaxy. We can therefore identify the true rotation velocity for this bin as that velocity for which the co-added spectrum has a velocity shift equal to the systemic velocity of the galaxy (as determined from the bins at smaller radii). In effect, this calculation is almost equivalent to simply co-adding all the spectra, measuring a mean velocity, and subtracting off the systemic velocity of the galaxy, but it is more accurate in that it does deal properly with the remaining corrections due to the varying projection into the line of sight of rotation velocity with azimuth.

Finally, the inner point in each rotation curve was derived by simply measuring the velocity shift (with respect to the galaxy’s systemic velocity) in the fibre closest to the centre of the galaxy. After correcting for the inclination of the galaxy and the azimuthal angle of the fibre, this gives a rotational velocity for the central fibre. Note, however, that the large diameter of the fibres causes a strong ‘beam smearing’ effect: due to the large velocity gradients in the centres of these galaxies, the central fibre probes stars with different velocities and the measured velocity shift is the result of a complicated convolution of the stellar velocity field and the brightness distribution. Thus, the central points in the rotation curves should only be used with caution.

The resulting rotation curves for the four galaxies in the sample are tabulated in Table 4 and plotted in black in Figure 4. The quoted radii are the luminosity-weighted average radii of all fibres in each bin.

### 4.3 Stellar velocity dispersions

The method described above to derive the stellar rotation curves also yields an average velocity dispersion for each radial ring. However, since the velocity dispersion tensor can be quite strongly anisotropic, and different azimuth angles give different projections of this tensor, we might expect the measured line-of-sight velocity dispersion to vary systematically with azimuth. To quantify this effect, we divided each radial bin in three sub-bins, according to the azimuthal angles of the fibres. For each radial bin, we combine all spectra within  $30^\circ$  of the major axis, between  $30$  and  $60^\circ$  from the major axis, and within  $30^\circ$  of the minor axis (all measured in the plane of the galaxy disc), as shown in Figure 2. Within each sub-bin, the individual spectra are shifted by an amount that subtracts out the rotational velocity derived above, as appropriate for that individual fibre’s azimuthal angle. The shifted spectra in the sub-bin are then co-added with no weighting, and the velocity dispersion derived for the composite spectrum.

The resulting profiles of velocity dispersion along the major, intermediate and minor axes are listed in Table 4 and plotted in Figure 4. The radii are, again, the luminosity weighted average radii of all fibres in each sub-bin; the small differences between the effective radii for the three sub-bins in a given radial bin reflect the details of the fibre locations



Table 4: Measured kinematic properties.

galaxy	$V_{\text{sys}}$		stellar rotation curve			stellar velocity dispersion profiles					
	This study	N07	$R_{\text{eff}}$ "	$V_{\text{rot}}$ $\text{km s}^{-1}$	method	major axis		intermediate		minor axis	
	$\text{km s}^{-1}$	$\text{km s}^{-1}$				$R_{\text{eff}}$ "	$\sigma_{\text{maj}}$ $\text{km s}^{-1}$	$R_{\text{eff}}$ "	$\sigma_{\text{int}}$ $\text{km s}^{-1}$	$R_{\text{eff}}$ "	$\sigma_{\text{min}}$ $\text{km s}^{-1}$
NGC 2273	$1837.9 \pm 1.0$	1837	1.8	$104.2 \pm 18.8$	central fibre	1.8	$121.0 \pm 2.6$	1.8	$121.0 \pm 2.6$	1.8	$121.0 \pm 2.6$
			5.2	$127.6 \pm 2.2$	minimum dispersion	4.1	$114.1 \pm 2.8$	6.5	$116.0 \pm 3.8$	5.8	$120.2 \pm 2.8$
			12.2	$173.0 \pm 2.6$	minimum dispersion	12.0	$103.5 \pm 4.2$	12.2	$111.5 \pm 2.6$	12.2	$117.2 \pm 2.5$
			20.6	$211.7 \pm 1.7$	minimum dispersion	20.7	$41.6 \pm 1.9$	20.6	$60.6 \pm 1.9$	20.4	$79.9 \pm 1.6$
			29.4	$200.8 \pm 1.8$	minimum dispersion	29.1	$34.6 \pm 2.1$	29.8	$43.5 \pm 1.6$	29.3	$55.6 \pm 1.6$
			48.1	$196.6 \pm 2.6$	minimum dispersion	53.4	$26.7 \pm 5.4$	48.5	$32.9 \pm 2.9$	44.8	$51.5 \pm 2.2$
			79.3	$184.8 \pm 11.5$	velocity shift	–	–	80.5	$21.3 \pm 23.8$	–	–
			–	–	–	–	–	–	–	–	–
NGC 2985	$1325.0 \pm 4.9$	1329	1.3	$30.2 \pm 8.6$	central fibre	1.3	$141.5 \pm 2.0$	1.3	$141.5 \pm 2.0$	1.3	$141.5 \pm 2.0$
			3.8	$102.4 \pm 8.3$	minimum dispersion	4.7	$136.1 \pm 2.3$	3.2	$139.3 \pm 1.5$	4.5	$133.9 \pm 2.5$
			8.1	$182.2 \pm 8.5$	minimum dispersion	8.9	$126.3 \pm 3.3$	7.5	$127.8 \pm 2.5$	8.2	$117.5 \pm 1.8$
			13.8	$163.4 \pm 13.3$	velocity shift	14.4	$108.4 \pm 3.4$	13.4	$105.3 \pm 3.1$	13.7	$100.1 \pm 1.8$
			20.4	$200.5 \pm 11.3$	velocity shift	20.6	$77.8 \pm 2.8$	20.8	$100.1 \pm 3.6$	20.1	$97.7 \pm 2.6$
			29.0	$210.1 \pm 10.7$	velocity shift	29.6	$71.5 \pm 3.3$	29.0	$87.8 \pm 3.0$	28.4	$92.4 \pm 3.2$
			44.7	$219.2 \pm 10.5$	velocity shift	46.4	$70.5 \pm 3.8$	43.7	$72.6 \pm 4.5$	40.8	$95.7 \pm 8.1$
			62.0	$220.2 \pm 10.8$	velocity shift	62.0	$62.3 \pm 4.7$	–	–	–	–
			79.8	$216.1 \pm 12.5$	velocity shift	79.8	$58.8 \pm 6.9$	–	–	–	–
			99.1	$222.9 \pm 31.2$	velocity shift	99.1	$62.1 \pm 23.2$	–	–	–	–
NGC 3898	$1171.9 \pm 2.5$	1172	1.2	$9.3 \pm 3.1$	central fibre	1.2	$221.4 \pm 2.0$	1.2	$221.4 \pm 2.0$	1.2	$221.4 \pm 2.0$
			6.5	$137.9 \pm 3.1$	minimum dispersion	7.8	$173.3 \pm 3.4$	5.4	$184.9 \pm 1.7$	8.2	$181.9 \pm 2.8$
			12.5	$190.2 \pm 3.1$	minimum dispersion	11.9	$143.1 \pm 3.5$	12.6	$150.3 \pm 2.7$	12.7	$158.9 \pm 2.4$
			19.6	$154.9 \pm 7.2$	velocity shift	20.0	$137.1 \pm 4.0$	20.3	$141.2 \pm 3.2$	19.2	$143.0 \pm 2.0$
			35.3	$148.7 \pm 7.2$	velocity shift	36.0	$152.0 \pm 7.7$	36.3	$152.7 \pm 4.1$	34.7	$149.8 \pm 2.6$
			54.9	$166.3 \pm 6.5$	velocity shift	54.1	$119.4 \pm 6.5$	55.6	$131.8 \pm 7.7$	55.0	$141.0 \pm 4.9$
			71.1	$153.4 \pm 8.1$	velocity shift	71.3	$125.3 \pm 9.8$	70.8	$121.2 \pm 7.0$	71.1	$160.0 \pm 7.1$
			95.5	$108.4 \pm 27.2$	velocity shift	–	–	–	–	88.2	$133.1 \pm 12.3$
NGC 5533	$3847.6 \pm 2.2$	3858	1.5	$95.4 \pm 3.7$	central fibre	1.5	$143.4 \pm 2.2$	1.5	$143.4 \pm 2.2$	1.5	$143.4 \pm 2.2$
			4.6	$184.5 \pm 3.2$	minimum dispersion	3.3	$141.1 \pm 1.7$	6.0	$137.5 \pm 2.7$	5.4	$139.4 \pm 2.2$
			10.9	$224.1 \pm 3.7$	minimum dispersion	10.4	$108.7 \pm 2.9$	11.1	$121.6 \pm 2.6$	11.3	$122.7 \pm 3.6$
			19.8	$241.4 \pm 3.7$	minimum dispersion	19.7	$106.6 \pm 3.3$	20.1	$112.6 \pm 4.1$	19.6	$110.4 \pm 3.8$
			31.6	$219.3 \pm 4.3$	minimum dispersion	31.0	$102.0 \pm 4.7$	31.7	$92.2 \pm 3.3$	32.0	$104.5 \pm 5.4$
			52.1	$208.4 \pm 6.2$	minimum dispersion	55.0	$69.4 \pm 8.9$	53.4	$54.1 \pm 6.5$	46.4	$91.2 \pm 8.9$
			76.5	$174.3 \pm 16.8$	velocity shift	76.4	$56.8 \pm 24.4$	76.7	$30.5 \pm 19.7$	–	–
			–	–	–	–	–	–	–	–	–

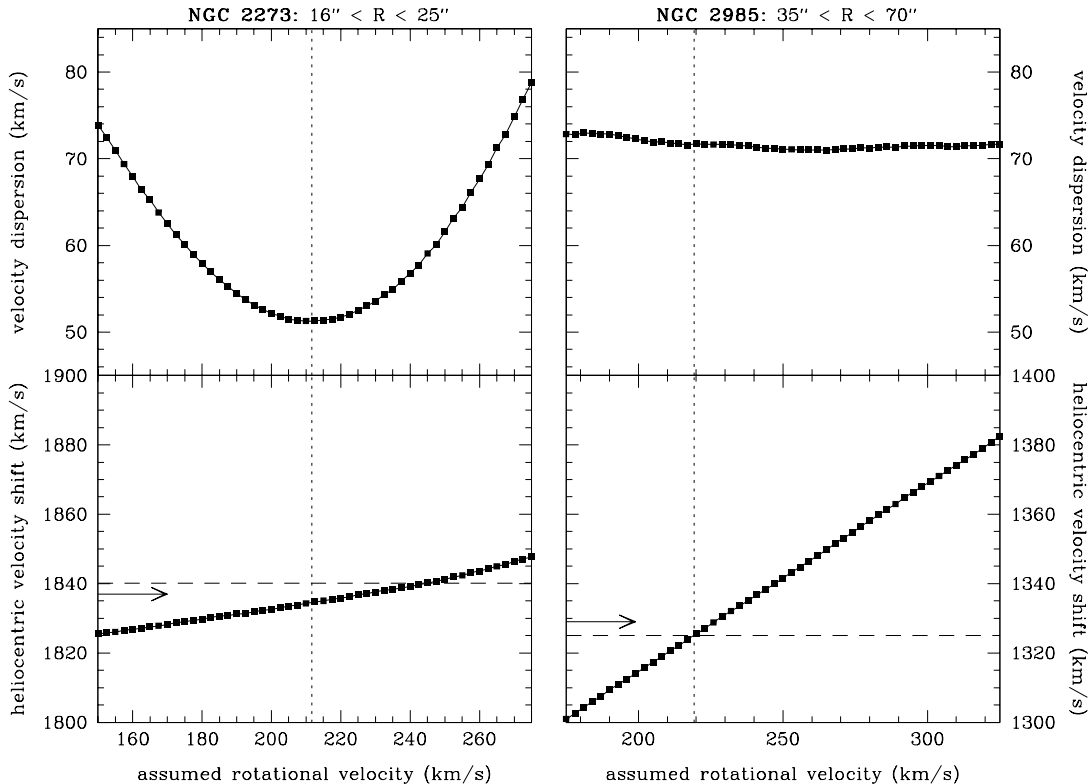


**Figure 3.** Illustration of the procedure used to measure the stellar rotational velocities. The top left hand panel shows the measured velocity dispersion for the spectra at intermediate radii ( $16'' < R < 25''$ ) in NGC 2273, as a function of assumed rotational velocity. The bottom left hand panel shows the corresponding velocity shifts. The right hand panels show the same data for the spectra at larger radii ( $35'' < R < 70''$ ) in NGC 2985. The vertical, dotted lines indicate the deduced rotational velocities. The horizontal dashed lines in the bottom panels indicate the derived systemic velocity of each galaxy; the arrows indicate the corresponding value from N07.

and brightness distribution of each galaxy. Generally speaking, these velocity dispersion profiles are well behaved in the sense that they vary smoothly with radius, and show a systematic ordering in amplitude between minor, intermediate and major axes, characteristic of the detection of an anisotropic velocity dispersion. The orderliness of these data must to some extent be due to the particularly simple featureless early-type disks selected for this sample, but it also reflects the care taken in obtaining the data and analyzing it in an optimal manner.

## 5 MODELLING THE DYNAMICS

Having obtained these high-quality kinematic data, we are now in a position to begin to interpret them both qualitatively and quantitatively in terms of the galaxies' stellar dynamics. An interesting qualitative diagnostic comes from plotting the ratio of velocity dispersions along major and minor axes versus radius. As Figure 5 shows, this plot confirms that the velocity dispersions show an orderly variation with radius. Inclusion of the ratio of the intermediate-angle velocity dispersion to the major axis dispersion on this plot further confirms the orderliness of the data. For NGC 3898 and NGC 5533, the data show no evidence that these ratios depart from unity, consistent with an isotropic velocity dispersion tensor. This simplicity could well be associated with the ‘‘hotness’’ of the disks in these systems, particu-

larly in the case of NGC 3898 where random motions remain comparable to rotational ones at all radii: as indicated by Merrifield et al. (2001) and Shapiro et al. (2003), earlier-type galaxies, which typically have hotter disks, also tend to have simpler more isotropic velocity dispersions.

The behaviour for NGC 2273 and NGC 2985 is more interesting. At small radii, these systems display the isotropic velocity dispersions that one would expect for the centre of a hot-bulge stellar population. However, they undergo what appears to be a quite sudden transition to a different regime in which the minor axis dispersion exceeds the major axis one. Since the minor-axis line-of-sight velocity dispersion contains a large component of the radial intrinsic velocity dispersion, while the major-axis line-of-sight velocity dispersion is dominated by the azimuthal intrinsic velocity dispersion, this departure from unity would indicate that in the outer regions of these galaxies the velocity dispersion tensor is radially anisotropic.

Such anisotropy is expected in a colder disk population, so this transition seems a fairly clear indicator of a transition from the bulge to disk in these systems. However, comparison with Figure 4 shows that any such naive decomposition into bulge and disk should be treated with some caution, as the radius at which this transition in the velocity dispersion tensor occurs does not correspond to the radius at which the photometric decomposition indicates a transition from bulge to disk, nor does it occur near the radius at which rotational motion starts to dominate over random motions. The

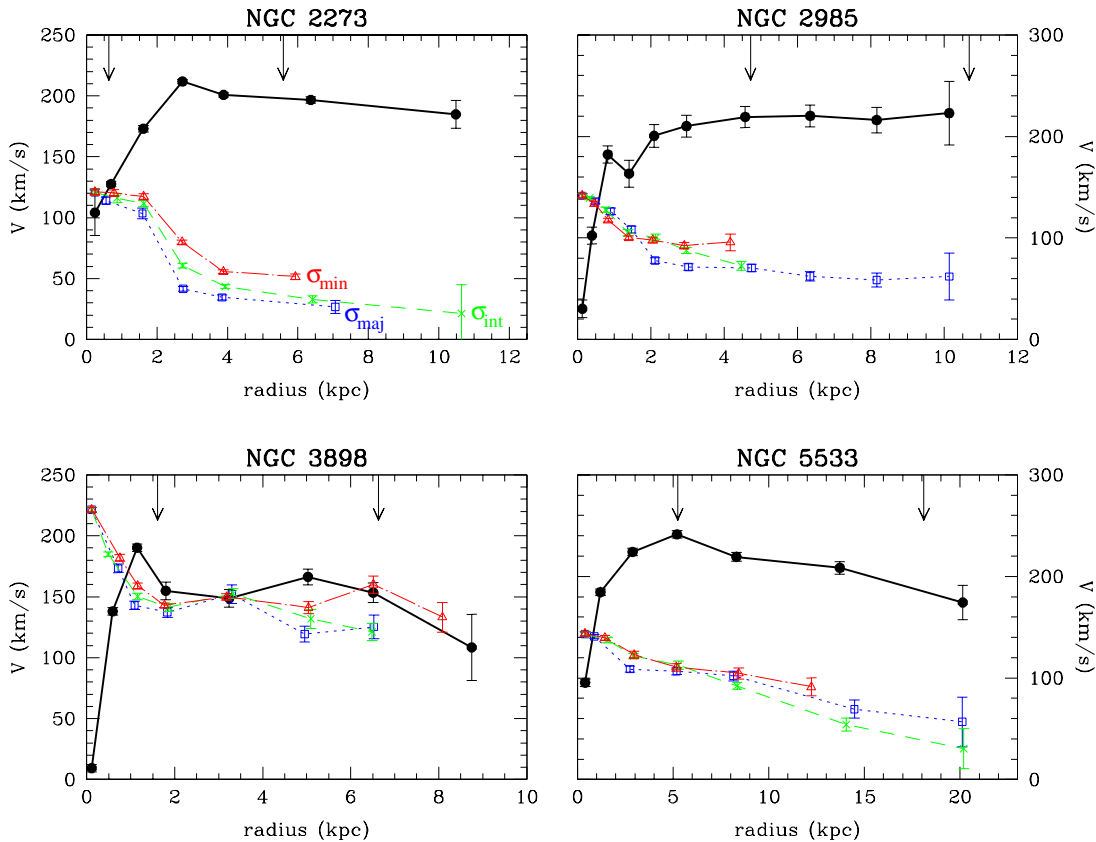


**Figure 4.** Stellar rotation curves and velocity dispersion profiles. Bold lines and bullets show the stellar rotation curves. Squares connected by dotted lines, crosses connected by dashed lines and triangles connected by dot-dashed lines indicate the velocity dispersions along the major, intermediate and minor axes respectively. Error bars show the formal measurement errors (see Section 4.1 for details). The inner vertical arrows indicate the transition radius between bulge and disc dominated photometry, while the outer arrows indicate two disc scale lengths.

lack of correspondence between the kinematic and photometric decompositions provides a health warning about the lack of uniqueness in the photometric approach, reflecting the loss of information when the full dynamical phase space is not accessible. The lack of correspondence between the transition to disk-like kinematics and the radius at which rotational motion dominates is more interesting, and presumably reflects the more complex nature of the internal dynamics of these systems. It is, however, notable that the transition in the velocity dispersions does correspond closely to the radius at which the rotational motion flattens out to its approximately-constant asymptotic value, which is also the regime in which one would expect the dynamics to take on a relatively simple disk-like form.

### 5.1 Asymmetric drift

We now turn to more quantitative consideration of the dynamics of these systems, specifically seeking to understand whether the stellar motions respect the asymmetric drift equation, as we might expect. This equation, which quantifies the lag due to random stellar motions between mean rotational motion and the local circular speed, can be written

$$V_c^2 = V_{\text{rot}}^2 + \sigma_\phi^2 - \sigma_R^2 \left( 1 + \frac{d(\ln \nu)}{d(\ln R)} \right) - R \frac{d\sigma_R^2}{dR}. \quad (1)$$

where  $V_c$  is the local circular speed,  $V_{\text{rot}}$  is the measured rotational velocity of the stars at this radius,  $\sigma_\phi$  and  $\sigma_R$  are the azimuthal and radial components of the velocity dispersion ellipsoid and  $\nu$  is the stellar number density (Binney & Tremaine 1987). In this formulation, we have followed the usual procedure of neglecting the tilt term,  $d(\overline{V_R V_z})/dz$ , which is assumed to be small compared to the other terms.

The intrinsic components of velocity dispersion,  $\sigma_\phi$  and  $\sigma_R$ , are related to the observed major- and minor-axis velocity dispersions by the relations

$$\begin{aligned} \sigma_{\text{maj}}^2 &= \sigma_\phi^2 \sin^2 i + \sigma_z^2 \cos^2 i \\ \sigma_{\text{min}}^2 &= \sigma_R^2 \sin^2 i + \sigma_z^2 \cos^2 i, \end{aligned} \quad (2)$$

which also include the contributions from the velocity dispersion in the third, vertical, direction,  $\sigma_z$ . Without additional information, one cannot derive all three components of the velocity dispersion from these two observed quantities. However, three of the four galaxies in this sample are sufficiently close to edge-on that very little of the vertical motion projects into the line of sight (we return to the fourth, NGC 2985, below). For these galaxies, the assumed behaviour of this third component has very little impact on the inferred values for the other two components. For simplicity, and motivated by the apparent isotropy in two of these galaxies, we therefore make the simplest possible as-

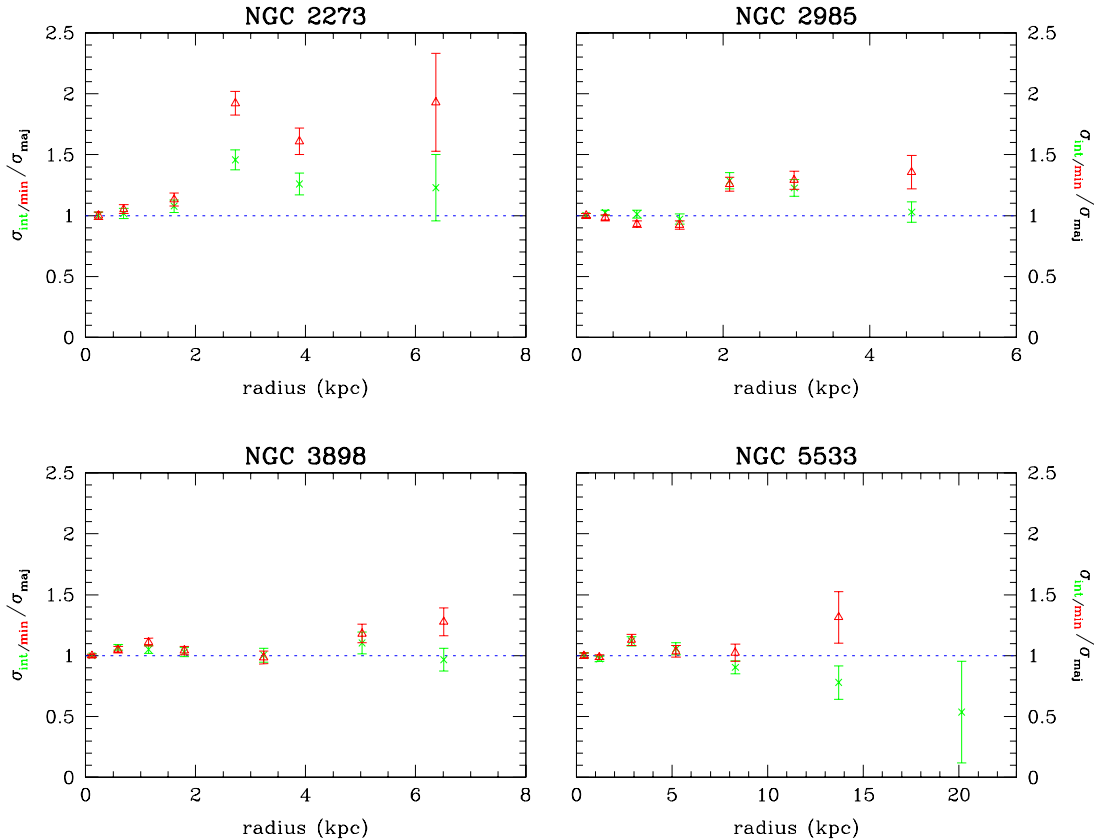


**Figure 5.** Ratios of observed velocity dispersions as a function of radius. The red triangles and green crosses show, respectively, the ratio of the velocity dispersions along the minor and intermediate axes to those on the major axis.

sumption that  $\sigma_z = \sigma_\phi$ . Under this assumption, equation 2 reduces to:

$$\begin{aligned} \sigma_\phi &= \sigma_{\text{maj}} \\ \sigma_R &= \sqrt{\frac{\sigma_{\text{min}}^2 - \sigma_{\text{maj}}^2 \cos^2 i}{\sin^2 i}}. \end{aligned} \quad (3)$$

The profiles for  $\sigma_\phi$  and  $\sigma_R$  obtained from this equation are shown in Figure 6. For radii where we have not measured  $\sigma_{\text{maj}}$  or  $\sigma_{\text{min}}$  (but where we have at least one of  $\sigma_{\text{maj}}$ ,  $\sigma_{\text{int}}$  or  $\sigma_{\text{min}}$ ), we use the fact that the ratios of these quantities as shown in Figure 5 are consistent with remaining constant at large radii, in order to extrapolate values.

Equation 1 also requires the density of the stellar tracer,  $\nu(R)$ , which we obtain directly from the R-band photometric profiles from Noordermeer & van der Hulst (2007). Such red light traces the stellar population whose kinematics we are measuring here quite closely, although for such early-type disk galaxies, which contain little by way of colour gradients, the choice of band is not critical. More challengingly, equation 1 also demands a measure of the radial gradient in the velocity dispersion. Motivated by a number of previous observations (e.g. van der Kruit & Freeman 1986; Lewis & Freeman 1989; Bottema 1993), this derivative has conventionally been obtained by assuming that the profile declines exponentially (Gerssen et al. 1997; Westfall et al. 2008). However, it is apparent from Figure 6 that these higher-quality data are really not consistent with such a simple assumed form – a point also uncovered in other recent

studies of velocity dispersion profiles in disk galaxies (e.g. Merrett et al. 2006; Noordermeer et al. 2008). Accordingly, we have adopted the less parametric approach of interpolating the velocity dispersion profile on to a polynomial and calculating its derivative numerically. Such a procedure will tend to amplify any noise in the data, but such noise amplification represents the true uncertainty that arises from the presence of this derivative in the equation, so is an honest and unbiased way to include this term in the calculation.

Inserting all these ingredients into equation 1 allows us to solve for the circular velocity as a function of radius in these galaxies,  $V_c(R)$ , as shown in Figure 6. As described above, we can compare these inferred values to the rotation curves obtained directly from emission-line data, which are also shown in Figure 6. On the whole, the derived rotation curves match reasonably well, in that the correction for asymmetric drift shifts the stellar streaming data significantly closer to the true rotation curve, and in several cases provides an almost-exact match. The only real exception is NGC 2273, where the asymmetric drift correction over-enhances the inferred rotation curve modestly above its true value. It is notable that this is by far the coldest disk system in the sample, and as such it is most likely to fall victim to any residual systematic errors that will tend to over-estimate the velocity dispersions and hence over-correct for asymmetric drift. However, for such a system the asymmetric drift correction is in any case small, so the associated small bias does not have a large impact on the inferred rotation curve. The last point in the NGC 3898 data is also high,

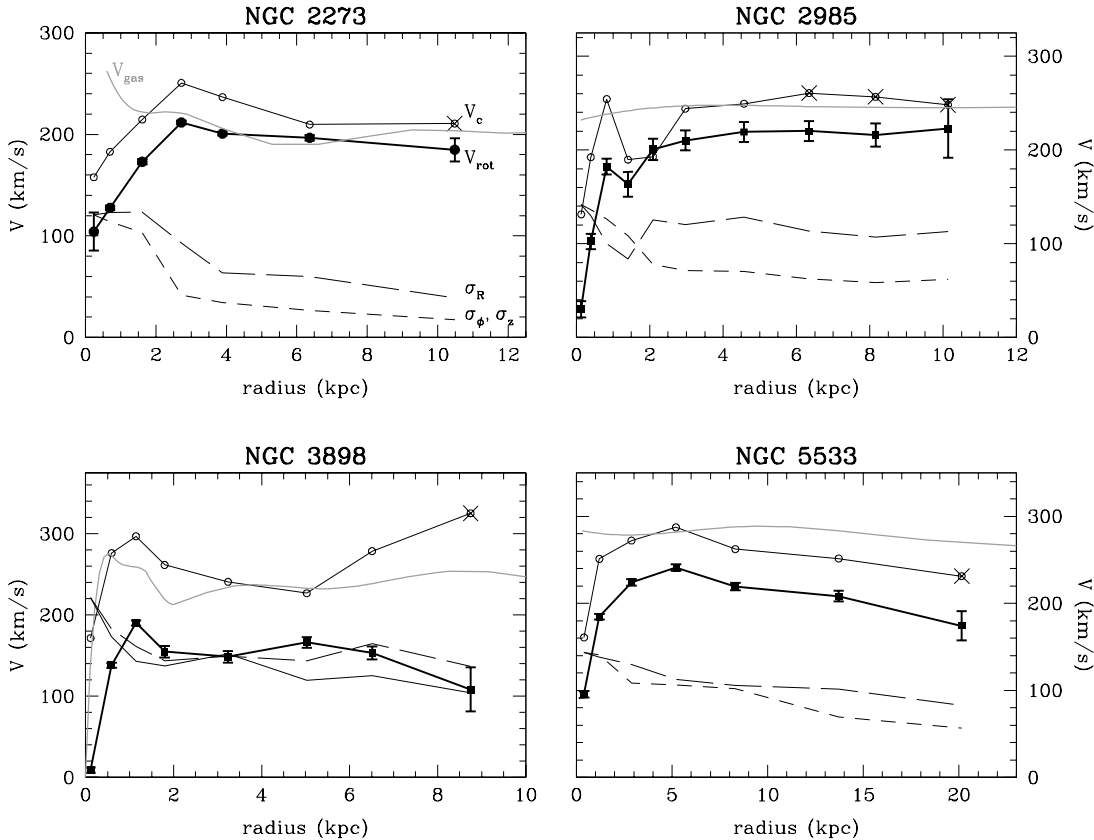


**Figure 6.** Derived dynamical properties of the sample galaxies. Bold lines and bullets show the raw rotational velocities (as in Figure 4), while thin solid lines and open symbols show the stellar rotation curves after correction for asymmetric drift using equations 1 and 3. Crosses indicate points where the velocity dispersions were not measured along all three axes. Grey lines show the gas rotation curves from N07. Short and long dashed lines show, respectively, the azimuthal and radial components of the velocity dispersion ellipsoid.

but the error bars are large, and the derivative term has a very large uncertainty without bracketing data from which to interpolate. Even when the asymmetric drift term is large, both in the bulge-dominated regions of all the systems and the outer parts of those with hot disks, the inferred rotation curve matches the true one reasonably well, which bodes well for the application of such corrections to generally-hot S0 systems that lack the external measure of the rotation curve afforded by emission-line data.

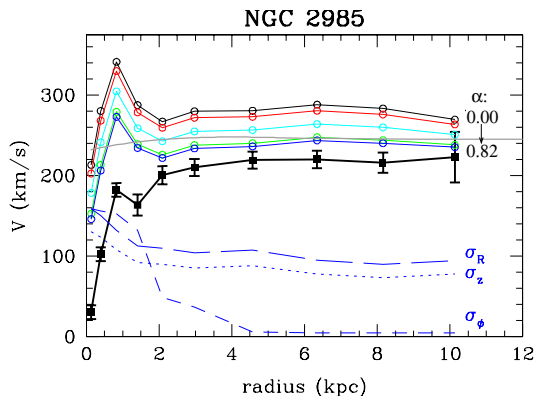
Note that the ansatz that  $\sigma_z = \sigma_\phi$  had no real physical basis. In fact, it would be dynamically more interesting to investigate whether the data are consistent with  $\sigma_z = \sigma_R$ , as such an equality is required if the underlying distribution function respects only two integrals of motion (Jeans 1915). As described above, most of the galaxies are sufficiently far from face-on that different assumptions about  $\sigma_z$  make little difference to the observables. However, NGC 2985 is close enough to face-on for a significant amount of motions perpendicular to the plane to project into the line of sight, so for this galaxy we can investigate the behaviour of  $\sigma_z$ , and hence test this possibility.

Figure 7 shows the corrected rotation curves for a range of different values adopted for the ratio  $\alpha = \sigma_z/\sigma_R$ , ranging from  $\alpha = 0$  to  $\alpha = 0.82$ . It turns out that  $\alpha = 0.82$  is the maximum possible value, since at this value  $\sigma_z$  is responsible for all the observed velocity dispersion along the major axis, so  $\sigma_\phi$  goes to zero (see Figure 7). Any larger value for

$\alpha$  would further increase  $\sigma_z$ , making  $\sigma_\phi$  unphysically imaginary (see equation 2). Thus, we can robustly rule out the possibility that  $\sigma_z = \sigma_R$  in this system: perhaps unsurprisingly, the disk distribution function in NGC 2985 requires a third integral.

Clearly, even pushing  $\alpha$  as high as 0.82 results in a physically implausible model with zero velocity dispersion in the tangential direction. It also conflicts with the observations in that, as Figure 7 shows, it fails to reproduce the emission-line-derived rotation curve. From this additional constraint, one can see that for a model to match this observation we require a value of  $\sigma_z/\sigma_R$  of approximately 0.7. In fact, the ratio is essentially identical to the model shown in Figure 6, since for this new model it also turns out that  $\sigma_z \approx \sigma_\phi$ , as previously assumed. By using this additional constraint of requiring the observed asymmetric drift to be reproduced, as well as the two observed components of velocity dispersion, we have effectively closed the system to show that the velocity ellipsoid in the disk of this system, if its shape is approximately constant with radius, must have principal axes in the ratio  $\sigma_z : \sigma_\phi : \sigma_R \approx 0.7 : 0.7 : 1$ .

This ratio is instructive because the rotation curve for NGC 2985 is very close to being flat, for which the epicyclic approximation would also predict a value of  $\sigma_\phi/\sigma_R = 1/\sqrt{2} \approx 0.7$ , quite independent of the above analysis. At least for this system, it would appear that the concerns over the validity of the epicyclic approximation are unfounded,



**Figure 7.** The effect of varying assumptions for the vertical velocity dispersion on the corrections for asymmetric drift in NGC 2985. The bold line and bullets show the raw rotational velocities of the stars (as in Figure 4) and the gray line shows the gaseous rotation curve from N07. The thin black, red, cyan, green and blue lines and open circles show the rotation curves, corrected for asymmetric drift assuming ratios of vertical-to-radial velocity dispersion of respectively  $\alpha = 0, 0.25, 0.5, 0.75$  and  $0.82$ . The blue dotted, long and short dashed lines show the profiles of the vertical, radial and tangential velocity dispersion for the limiting case of  $\alpha = 0.82$ .

providing more confidence in its use for systems even where the ratio of ordered-to-random velocities is as low as  $\sim 3$ .

## 6 CONCLUSIONS

In this paper, we have presented deep IFU observations of four nearby early-type disk galaxies with good emission-line rotation curves. These high-quality data were obtained with the motivation both of developing new techniques for the optimal extraction of kinematic parameters, and of testing the frequently-adopted dynamical formulae of the asymmetric drift equation and the epicyclic approximation. The conclusions of this study are as follows:

- With care, it is possible to extract the rather subtle dynamical signature of a disk system from two-dimensional spectral data. In particular, one can avoid the biases produced by the artificial enhancement of velocity dispersion that occurs when data are inappropriately averaged together.

- With such data, application of the asymmetric drift equation seems to work reasonably well, in that one can reproduce the rotation curve as inferred independently from emission-line data. There is a caveat that residual systematic errors may compromise the results to some extent for particularly cold systems, but for such systems the asymmetric drift corrections are small, so the corresponding small bias is not too debilitating. For hotter systems, the inferred accuracy of the correction is important for the credibility of the rotation speeds inferred for S0 galaxies in studies of their Tully–Fisher relation, as one does not usually have the luxury of an emission-line rotation curve in such systems.

- For an appropriately-inclined system like NGC 2985, one can obtain a strong upper limit on the ratio of  $\sigma_z/\sigma_R$ , which rules out the possibility that the system only respects two integrals of motion.

- Such data, combined with the asymmetric drift equation, allow one to solve for the full three-dimensional shape of the velocity dispersion tensor. In the case of NGC 2985, even though it is a relatively-hot early-type disk, the resulting ratio of velocity dispersions is quite consistent with the prediction of simple epicyclic theory, giving some further confidence in the general applicability of this approximation.

Clearly, with the development of large-field high-dispersion IFUs like PPAK, it is now possible to map out the kinematics of nearby disk galaxies in great detail, and hopefully this paper has demonstrated that it is possible to analyze such data and model them using the appropriate dynamical equations, with the aim of understanding their full phase-space structure, and, ultimately, their formation.

## ACKNOWLEDGEMENTS

We are greatly indebted to Marc Verheijen, for his help in the preparation of the observations as well as the data reduction, and Alejandro Bedregal for his advice on the analysis and interpretation of the spectra. We would also like to thank the staff at the Calar Alto Observatory for their assistance during the observations and the data reduction. This work is based on observations collected at the Centro Astronómico Hispano Alemán (CAHA) at Calar Alto, operated jointly by the Max-Planck Institut für Astronomie and the Instituto de Astrofísica de Andalucía (CSIC). The observations were funded by the Optical Infrared Coordination Network (OPTICON), a major international collaboration supported by the Research Infrastructures Programme of the European Commission’s Sixth Framework Programme. MRM gratefully acknowledges the support of a PPARC/STFC Senior Fellowship.

## REFERENCES

- Bedregal A. G., Aragón-Salamanca A., Merrifield M. R., 2006, *MNRAS*, 373, 1125
- Bedregal A. G., Aragón-Salamanca A., Merrifield M. R., Milvang-Jensen B., 2006, *MNRAS*, 371, 1912
- Binney J., Tremaine S., 1987, *Galactic dynamics*. Princeton, NJ, Princeton University Press, 1987
- Bottema R., 1993, *A&A*, 275, 16
- Bottema R., van der Kruit P. C., Freeman K. C., 1987, *A&A*, 178, 77
- Cappellari M., Emsellem E., 2004, *PASP*, 116, 138
- Emsellem E., Cappellari M., Peletier R. F., McDermid R. M., Bacon R., Bureau M., Copin Y., Davies R. L., Krajnović D., Kuntschner H., Miller B. W., Tim de Zeeuw P., 2004, *MNRAS*, 352, 721
- Gerssen J., Kuijken K., Merrifield M. R., 1997, *MNRAS*, 288, 618
- Jeans J. H., 1915, *MNRAS*, 76, 70
- Kelz A., Verheijen M. A. W., Roth M. M., Bauer S. M., Becker T., Paschke J., Popow E., Sánchez S. F., Laux U., 2006, *PASP*, 118, 129
- Kuijken K., Tremaine S., 1994, *ApJ*, 421, 178
- Lewis J. R., Freeman K. C., 1989, *AJ*, 97, 139
- Merrett H. R., Merrifield M. R., Douglas N. G., Kuijken K., Romanowsky A. J., Napolitano N. R., Arnaboldi M.,

- Capaccioli M., Freeman K. C., Gerhard O., Coccatto L., Carter D., Evans N. W., Wilkinson M. I., Halliday C., Bridges T. J., 2006, *MNRAS*, 369, 120
- Merrifield M. R., Gerssen J., Kuijken K., 2001, in Funes J. G., Corsini E. M., eds, *Galaxy Disks and Disk Galaxies* Vol. 230 of *Astronomical Society of the Pacific Conference Series*, *The Origins of Disk Heating*. pp 221–224
- Noordermeer E., Merrifield M. R., Coccatto L., Arnaboldi M., Capaccioli M., Douglas N. G., Freeman K. C., Gerhard O., Kuijken K., de Lorenzi F., Napolitano N. R., Romanowsky A. J., 2008, *MNRAS*, 384, 943
- Noordermeer E., van der Hulst J. M., 2007, *MNRAS*, 376, 1480
- Noordermeer E., van der Hulst J. M., Sancisi R., Swaters R. A., van Albada T. S., 2005, *A&A*, 442, 137
- Noordermeer E., van der Hulst J. M., Sancisi R., Swaters R. S., van Albada T. S., 2007, *MNRAS*, 376, 1513
- Roth M. M., Kelz A., Fechner T., Hahn T., Bauer S.-M., Becker T., Böhm P., Christensen L., Dionies F., Paschke J., Popow E., Wolter D., Schmoll J., Laux U., Altmann W., 2005, *PASP*, 117, 620
- Sánchez S. F., 2004, *Astronomische Nachrichten*, 325, 167
- Shapiro K. L., Gerssen J., van der Marel R. P., 2003, *AJ*, 126, 2707
- van der Kruit P. C., Freeman K. C., 1986, *ApJ*, 303, 556
- van Dokkum P. G., 2001, *PASP*, 113, 1420
- Verheijen M. A. W., Bershady M. A., Andersen D. R., Swaters R. A., Westfall K., Kelz A., Roth M. M., 2004, *Astronomische Nachrichten*, 325, 151
- Westfall K. B., Bershady M. A., Verheijen M. A. W., Andersen D. R., Swaters R. A., 2008, *ArXiv e-prints*, 801